infrastructures

MDPI

Article

Urban Infrastructure Vulnerability to Climate-Induced Risks: A Probabilistic Modeling Approach Using Remote Sensing as a Tool in Urban Planning

Ignacio Rodríguez-Antuñano [1], Brais Barros [2], Joaquín Martínez-Sánchez [1] and Belén Riveiro [1,*]

[1] CINTECX, GeoTECH Group, Campus Universitario de Vigo, Universidade de Vigo, As Lagoas, Marcosende, 36310 Vigo, Spain; ignacio.rodriguez.antunano@uvigo.gal (I.R.-A.); joaquin.martinez@uvigo.gal (J.M.-S.)
[2] ICITECH, Universitat Politècnica de València, Camino de Vera s/n, 46022 Valencia, Spain; bbargon1@upv.es
* Correspondence: belenriveiro@uvigo.gal

Abstract: In our contemporary cities, infrastructures face a diverse range of risks, including those caused by climatic events. The availability of monitoring technologies such as remote sensing has opened up new possibilities to address or mitigate these risks. Satellite images allow the analysis of terrain over time, fostering probabilistic models to support the adoption of data-driven urban planning. This study focuses on the exploration of various satellite data sources, including nighttime land surface temperature (LST) from Landsat-8, as well as ground motion data derived from techniques such as MT-InSAR, Sentinel-1, and the proximity of urban infrastructure to water. Using information from the Local Climate Zones (LCZs) and the current land use of each building in the study area, the economic and climatic implications of any changes in the current features of the soil are evaluated. Through the construction of a Bayesian Network model, synthetic datasets are generated to identify areas and quantify risk in Barcelona. The results of this model were also compared with a Multiple Linear Regression model, concluding that the use of the Bayesian Network model provides crucial information for urban managers. It enables adopting proactive measures to reduce negative impacts on infrastructures by reducing or eliminating possible urban disparities.

Keywords: Bayesian network model; nighttime land surface temperature; multiple linear regression model; Mt-InSAR; multispectral and radar satellite images; local climate zones; ground motion; urban resilience

Citation: Rodríguez-Antuñano, I.; Barros, B.; Martínez-Sánchez, J.; Riveiro, B. Urban Infrastructure Vulnerability to Climate-Induced Risks: A Probabilistic Modeling Approach Using Remote Sensing as a Tool in Urban Planning. *Infrastructures* **2024**, *9*, 107. https://doi.org/10.3390/infrastructures9070107

Academic Editor: Youssef Diab

Received: 5 April 2024
Revised: 5 June 2024
Accepted: 19 June 2024
Published: 4 July 2024

1. Introduction

Disasters in cities around the world have highlighted the vulnerability of the built environment to a diverse range of threats and have prompted concerns about improving the resilience of cities [1]. Urban and architectural planning, management, and (re)design can play a crucial role in integrating disaster risk reduction activities into the built environment, addressing issues such as urban flood risk [2,3], the Urban Heat Island Effect [4,5], or urban infrastructure collapses [6–10], ensuring the comfort and safety of citizens [1].

The proactive preparation for all types of obstacles, whether sudden or slow in origin, expected or unexpected, is the now popular concept of resilience [11]. There is some pressure on urban planning to provide solutions in this way, where satellite-based remote sensing can help to overcome these obstacles [12]. Satellite-based remote sensing offers a long-term solution for monitoring landscape-scale land use and land cover change, as well as aid in the implementation of land management policies [13]. Through the synergy of satellite imagery (both radar and optical images), it is possible to conduct comprehensive monitoring of a territory, applying predictive measures through data analysis that help authorities apply protective measures and inhabitants improve their quality of life. Thus, the development of tools to assist decision makers in urban management is desirable.

In this context of urban design, planning, and management focused on urban resilience for the protection of its inhabitants, one of the topics that has most concerned urban researchers is the "urban heat island" (UHI) due to climate change [12]. Numerous studies have explored this topic. For example, the underlying relationship between city size and UHI intensity was demonstrated in several cities in North America and Europe as early as 1967 [14]. Heat-related mortality was found to be higher in city centers than in suburban areas through meteorological monitoring stations in and around Shanghai [15].

Many studies use land surface temperature (LST) as an indicator for detecting UHI through satellite images. For instance, the effects of UHI were identified in three suburban areas in Hong Kong using images from the Landsat TM and ASTER satellites in 2005 [16]. This approach has evolved over time, and recent studies have used machine learning techniques to generate high-resolution (30 m) LST images by merging data from Landsat TM, Landsat 8, and MODIS using the Flexible Spatiotemporal Data Fusion method (FSDAF) and Random Forest (RF) to detect UHI temperature increases from 2018 to 2019 in the city of Chengdu, China [17].

Through the calculation of nighttime LST using satellite images, Night Urban Heat Islands (NUHIs) can be detected [18]. Despite its great importance as one of the most significant health risk factors (since the materials used in the urban fabric have greater thermal inertia during the night), the study of urban heat islands occurring during the night is still underdeveloped [18]. Besides nighttime LST, which is more sensitive to urbanization processes, it is more suitable to study the UHI effect, and analyzing only daytime LST can lead to misleading results [19].

The study of land surface temperature (LST) with multispectral satellite images can be complemented with other relevant information to investigate other urban risks that may affect citizens, such as the stability of urban infrastructure, allowing common risk areas to be identified.

Locating and predicting unstable areas in the city is now possible thanks to satellite radar imagery and InSAR technology. This technology maps subtle surface movements, thus enabling the condition of urban infrastructures to be monitored [20,21]. Early prediction of unstable areas is vital for efficient evacuations and infrastructure protection, reducing the risk to human lives and critical assets. Understanding and mapping unstable areas are applied across diverse fields such as land use, engineering design, and emergency planning to effectively mitigate climate-related risks [22]. Unstable patterns that anticipated collapses of different infrastructures have been detected with satellite radar imagery and InSAR technology [8,9,23,24]. Integrating this technology and its data into urban and architectural planning, design, and management can be crucial for reducing disaster risks in our cities and their infrastructures, ensuring that citizens are comfortable and safe.

Satellite radar imagery and InSAR technology also enable the investigation of potential risks due to extreme weather events like extreme rainfall or landslides [25]. High flood-risk areas were identified through ALOS PALSAR radar satellite images, as well as the determination of the presence of water bodies to assist decision makers in effective planning [26]. CNNs based on the intensity and coherence of the TerraSAR-X satellite images have been developed to map urban flooding [27]. A city-aware U-Net model was introduced using images of Sentinel-1 radar satellite multitemporal intensity and coherence to map flood extents in urban environments [28]. Through CNNs, an automatic building damage detection process has been developed from satellite imagery following natural disasters such as the Midwest floods [29]. Finally, in the mapping of effective predictors of urban flood hazard, distance to the waterway has been found to have the highest degree of importance [30,31].

Several studies have linked LST with information obtained from ground motion velocity and displacement using radar satellite images and the Mt-InSAR technique, for example, measuring the displacements of a dam and the evolution of its LST [32], the detection of subsidence caused by land dryness identified by LST [33], coincidence in burnt

areas identified by LST with subsidence areas [34], common risk of structural stability and anomalous temperature [35], detecting unstable areas in permafrost regions with lower mean annual LST [36], monitoring of the architectural heritage of Alba Iulia city in Romania through Landsat images collected between 1988 and 2019, and Sentinel images collected between 2018 and 2020. It identifies areas where authorities should focus to improve heritage conservation [37].

Through the information provided by Earth monitoring satellites, knowledge of these urban risks is attainable, enabling their mapping and analysis of relationships, becoming a powerful tool for urban managers. This allows them to "play" and discover the optimal city configuration, finding the best parameters among various values and factors, with the aim of promoting urban resilience and eliminating urban inequalities where several of these risks may occur in the same area and, therefore, a part of the city's population may be affected to a greater extent.

The study of a set of interrelated random variables (risks to the structural health of buildings measured through stability–instability caused by ground motion and climatic risks such as high land surface temperatures or distance from bodies of water with the intention of using it as a conditioning factor for extreme weather events such as extreme rainfall that may cause floods or landslides) can be performed by means of probabilistic techniques, such as Bayesian Networks, providing information to urban managers about what these relationships are like. These networks are based on graphical probabilistic models that use Directed Acyclic Graphs (DAGs), where nodes represent the random variables and edges denote the probabilistic dependencies between them [38]. Besides being sound in quantifying uncertainty, Bayesian Networks also enable the prediction of new data via inference. Bayesian Networks have been widely used in various fields of risk analysis [39–44]; land use change detection [45]; and constructing a mineral potential map [46].

To the best of our knowledge, there is no existing work that holistically combines Bayesian Networks with both multispectral and radar images, taking advantage of extreme weather events caused by climate change and ground motion information that those images provide, respectively, in order to identify risk zones or areas with urban inequalities (because several risks occur in the same area) as a tool for urban planning by analyzing the relationships that exist between these variables.

This study wants to enhance the use of satellite remote sensing by combining multispectral and radar imagery for urban research, with particular attention to risks that may arise in the city, both climatic and related to soil stability and individual infrastructures (buildings), depending on land coverage and use.

The main goal of this paper consists of quantifying the relationship between different urban variables: Local Climate Zones, the current land use of infrastructure and its proximity to water, the "nocturnal urban heat island" (NUHI) effect using nocturnal surface temperature (LST), and ground motion in the study area of Barcelona (Spain). These variables may represent the main urban and environmental hazards that have emerged in recent decades and which urban management can mitigate [47]. By constructing and comparing two models (Bayesian Networks and Multiple Linear Regression) using the aforementioned input variables, risk zones or areas where urban inequalities happen can be identified. These tools quantify the existing relationships among the variables studied.

For this purpose, this document consists of the following sections: in Section 2, the description of the case study (Barcelona) is presented. Section 3 includes the description of the data and their processing, as well as the methodology used. Section 4 presents the results, which are then discussed in Section 5, and Section 6 summarizes the main conclusions of the work.

2. Study Area and Resources

2.1. Study Area

The study area of Barcelona was chosen due to its dense urban infrastructure, which may be impacted by various extreme weather events associated with climate change. This makes it a good case study for developing urban design tools that can aid managers and urban planners in mitigating these effects.

Several preliminary studies have already been conducted in this geographical area both for climate assessments [18,48] in the Metropolitan Area of Barcelona (MAB), which have identified patterns of urban heat islands, and for the identification of infrastructure instabilities with subsidence in the area of the airport and port of Barcelona [49]. This work aims to bring this information together to create models that can be used as planning tools to address these risks. Our study expands the area of analysis beyond the MAB to include the boundaries defined by the 2018 Urban Atlas data for the Barcelona region.

2.2. Satellite Imagery and Additional Data Used

This study examines several inputs that can indicate the current climate emergency. It proposes the use of models that can serve as planning tools for the design of more sustainable and resilient urban areas, reducing the negative impact of cities and improving the quality of life of their inhabitants.

Two models were chosen for this study: a Bayesian Network and a Multiple Linear Regression. The dependent variables for both models were the ground motion velocity, while the explanatory variables were the Local Climate Zones (LCZ), the Current Use Code of buildings and their distance to water, the nighttime land surface temperature (LST), and the temperature difference between day and night (which both reveals the Urban Heat Island Effect at night). The selection of these data is driven by the intention to create models applicable to a diverse range of case studies, encompassing both coastal and noncoastal regions. The emphasis is on utilizing accessible data or data that can be generated with relative ease, making the methodology reproducible for any location worldwide.

The open-access data used in this analysis were acquired from various sources. The Landsat-8 and Sentinel-1 satellite data were obtained from the USGS National Land Imaging (NLI) Program and The Copernicus Open Access Hub, respectively. The land cover and land use datasets were sourced from the official WUDAPT data portal and the INSPIRE Cadastre Cartography QGIS plugin, respectively.

The Landsat-8 images consist of 11 spectral bands. Specifically, they include bands covering the visible, near-infrared, shortwave infrared, and thermal infrared regions of the electromagnetic spectrum [50]. This multiband dataset provides a wealth of information for land surface analysis, including vegetation indices, land cover classification, and, in our case, land surface temperature (LST) calculations.

For the analysis of nocturnal temperatures, the only available Landsat-8 nighttime image for the study area as of 28 August 2015 was used. To calculate the temperature difference with respect to the day, the daytime image of the same day (due to the significant presence of clouds in its coverage) was combined with the nearest cloud-free daytime image, in this case, the daytime image of 3 August 2015. These three images have a resolution of 100 m for bands 10 and 11, 15 m for band 8, and 30 m for the rest of their bands.

For the analysis of ground motion, we use the images of the Sentinel-1 radar satellite. Sentinel-1 operates in four exclusive acquisition modes in function of their spatial resolution/swath width: strip map mode (SM): 5 × 5 m/80 km; interferometric wide-swath mode (IW): 5 × 20 m/250 km (standard mode); extra-wide-swath mode (EW): 20 × 40 m/400 km; and wave mode (WV): 5 × 5 m/20 × 20 km. Moreover, the SM, IW, and EW operational modes can potentially produce four types of products in SAR: Level-0, Level-1 SLC, Level-1 GRD, and Level-2 OCN. Only WV operates in Level-2 OCN. Level-1 data are the generally available products intended for the majority of users. These data can be produced as Single-Look Complex (SLC) or as Ground Range Detected (GRD). Since the Single-Look Complex (SLC) keeps its phase information (which is essential to perform the MT-InSAR technique),

145 Single-Look Complex (SLC) Sentinel-1 radar images in interferometric wide-swath mode (IW) with a resolution of 20 m were selected in descending acquisition direction. The study period starts in 2018, as it is the latest year for which data are available in the latest Public Expenditure Assessment Report 2019 of the Independent Authority for Fiscal Responsibility (AIReF) [51]. The choice of study period (1 January 2018 to 31 October 2022) was based on the need to conduct an analysis as up to date as possible of the infrastructure and to discover any potential current risks that were previously unconsidered. The reference image for the analysis of Mt-InSAR is from 7 June 2020.

To better understand how the local climate is changing in a city based on its urban structure (i.e., building height, vegetation density, presence of bodies of water, amount of paved surfaces, etc.), we used the latest available version of The European LCZ map [52], which was last updated in March 2020. This map's data have a resolution of 100 m and are from the year 2016.

Finally, data on the current land use of the study area's buildings were obtained by direct download using the INSPIRE Cadastre Cartography QGIS plugin [53]. These data are continuously updated, as local cadastral authorities update them. The most recent data available are typically from the past few months or years, depending on the area and when the data were last updated. Additionally, their distance from bodies of water was obtained with the intention of using it as a conditioning factor for extreme weather events such as extreme rainfall that may cause floods or landslides.

This work relies on The European LCZ map. It was constructed by combining geospatial data and existing WUDAPT data with the intention of generating LCZ types and specific parameters for each country. This map has an 80% overall average accuracy, as reported in [52], making it a good cartographic base for identifying LCZ on a large scale.

The classification of urban areas into LCZ allows for a better understanding of how the local climate is changing in a city due to changes in its urban structure. This classification identifies ten types of LCZs for urbanized land and seven for natural land cover, based on building density, building height, ground surface area, and the proportion of green areas in the zone (for a better description of the definitions for Local Climate Zones used in this paper, we refer readers to the original source [54]).

Each Local Climate Zone has specific climatic characteristics, which may include temperature, humidity, wind speed, and air quality. The LCZ classification is used to identify urban climate patterns in a city and to aid in the development of strategies to reduce the impact of urban climate on human health and well-being.

Additionally, information on the current land use of each building in the study area is used to gain knowledge of both the property value and its safety. The distance of buildings to a body of water that may be affected by extreme weather events such as extreme rainfall that may cause floods or landslides due to climate change is also calculated.

All this information allows for a precise understanding of the economic and climatic repercussions of any modification of current soil characteristics.

3. Methodology

In this work, we present a methodology to explore the relationships between different factors associated with urban risk. The purpose is to develop models to assist urban decision makers. Our methodology is summarized in Figure 1, and it comprises four main phases: (1) obtaining environmental data and processing satellite images; (2) analysis of relationships between variables (correlation matrix); (3) construction of two predictive models, namely a Bayesian Network model and a Multiple Linear Regression model; (4) and prediction of ground motion velocity for the study area through the two models and comparison of their outputs.

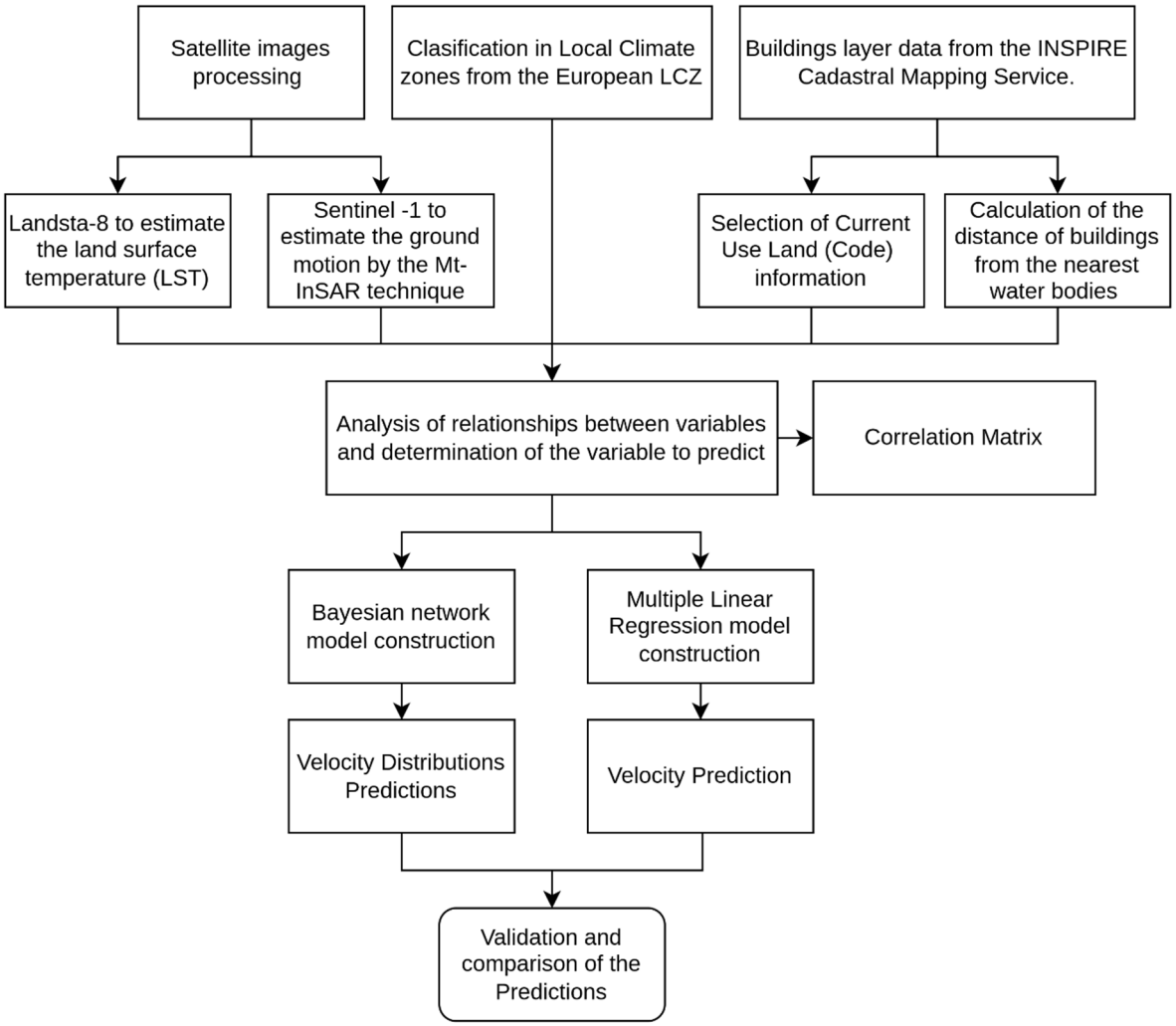

Figure 1. Workflow of the methodology proposed in this work.

3.1. Processing of Satellite Images

3.1.1. Estimation of Land Surface Temperature (LST)

Estimating land surface temperature (LST) at night provides additional knowledge about the urban heat island (UHI) due to its sensitivity to urbanization processes [19], especially during the so-called torrid nights that afflict cities. However, to date, the use of nocturnal LST is not yet common, among other factors, due to the scarce availability of satellite images with good resolution for this purpose. In our case study, we only have one image from August 2015 from the Landsat-8 satellite. The LST can be calculated using the top of atmosphere reflectance (R_λ) using Landsat-8 bands 4 and 5, surface emissivity (ε) using NDVI, and finally, the top of atmosphere radiance (L_λ) using Landsat-8 band 10. For a better description of the LST calculation used in this document, we refer readers to the original source of the plugin used [55]. In our case, we calculate the LST for both the nocturnal (nighttime temperatures) and diurnal (daytime temperatures) images on 28 August 2015, as well as the complementary image on 3 August 2015. With these three images, we calculate the difference in LST between daytime and nighttime to determine the thermal amplitude (LST Amplitude) that occurs in the study area. These patterns allow the detection of urban heat islands, indicating that during the day, the land surface temperature can be significantly higher than the surrounding surface temperature, while at night, the city's surface can retain heat and maintain higher temperatures than the surrounding areas. Therefore, the difference between diurnal and nocturnal LST (LST Amplitude) is used as an indicator of the magnitude of the urban heat island.

3.1.2. Ground Motion Using the Mt-InSAR Technique

Detecting infrastructure at risk due to land surface displacements is possible with the Mt-InSAR technique [56] and radar images through the Stanford Method (StaMPS). StaMPS is a type of processing technique and software package widely utilized in the processing of SAR data for Mt-InSAR applications. It focuses on identifying and tracking specific ground features (referred to as "persistent scatterers") that exhibit stable radar reflections over time. These features can be buildings, infrastructures, etc.

Therefore, Mt-InSAR (Multitemporal Interferometric Synthetic Aperture Radar) with StaMPS is a remote sensing technique used to measure ground motion and track its trend over years. It uses multiple time series of satellite radar images (synthetic aperture radar). The way to detect ground motion using the Mt-InSAR technique is that satellites emit a pulse of radar energy, this pulse is scattered over the earth's surface and recorded back at the satellite with two types of information: amplitude and phase. The amplitude is the strength of the return signal, influenced by the physical properties of the surface. The round-trip distance from the satellite to the ground is measured in units of radar wavelength, and changes in that distance between the time the radar images are collected are shown as a phase difference [57]. The advantage of Mt-InSAR is that it allows long-term monitoring of large areas with high spatial and temporal resolution, discovering millimeter-scale displacements.

In our case study, 146 images from Sentinel-1 were used. In this technique, the number of images used impacts the reliability of results, where the larger the number of images, the greater the accuracy obtained.

In Mt-InSAR processing, the phase change in the radar signal of images is compared in order to detect ground changes (phase differences). Particularly, one image is set as a reference image (Master), and the other images are called slaves. In our case study, the master image is dated 7 June 2020. The slaves comprise a dataset of images dated between 1 January 2018 and 31 October 2022.

3.2. Analysis of Relationships between Variables

The objective of this analysis is to understand the relationships that exist between the various inputs of information to address potential urban risks. To achieve this, the relationship between the study variables is measured using a correlation matrix (in Figure 2) that displays the correlation coefficients between all possible pairs of variables in the dataset. The correlation coefficient measures the strength and direction of the relationship between two variables to identify possible patterns or trends. In our study, we used the Spearman method, which measures the relationship between variables that are not necessarily linear but can be expressed through a monotonic increasing or decreasing function, that is, if the change in one variable is consistently associated with the change in the other variable. This method is often used when the variables do not follow a normal distribution or when the data contain outliers that may affect linear correlation. The Spearman method is also used for analyses where categorical data exist, as is the case with two variables in our study, LCZ and Current Use Code.

In this study, the use of a longer time scale, such as Landsat-8 daytime LST, would have enhanced the consistency of the results. Given the nature of the work focused on bridging the research gap in nighttime LST and nighttime UHI, the choice of using nighttime Landsat-8 imagery to analyze the relationship between land surface temperature and ground motion is justified. Despite the limited availability of nighttime data and only one image in the paper, the significant correlation (0.69) supports its use in the models. This provides a solid basis for the formulation of land management policies in the face of climate change, particularly focused on nighttime data (nighttime LST and nighttime UHI).

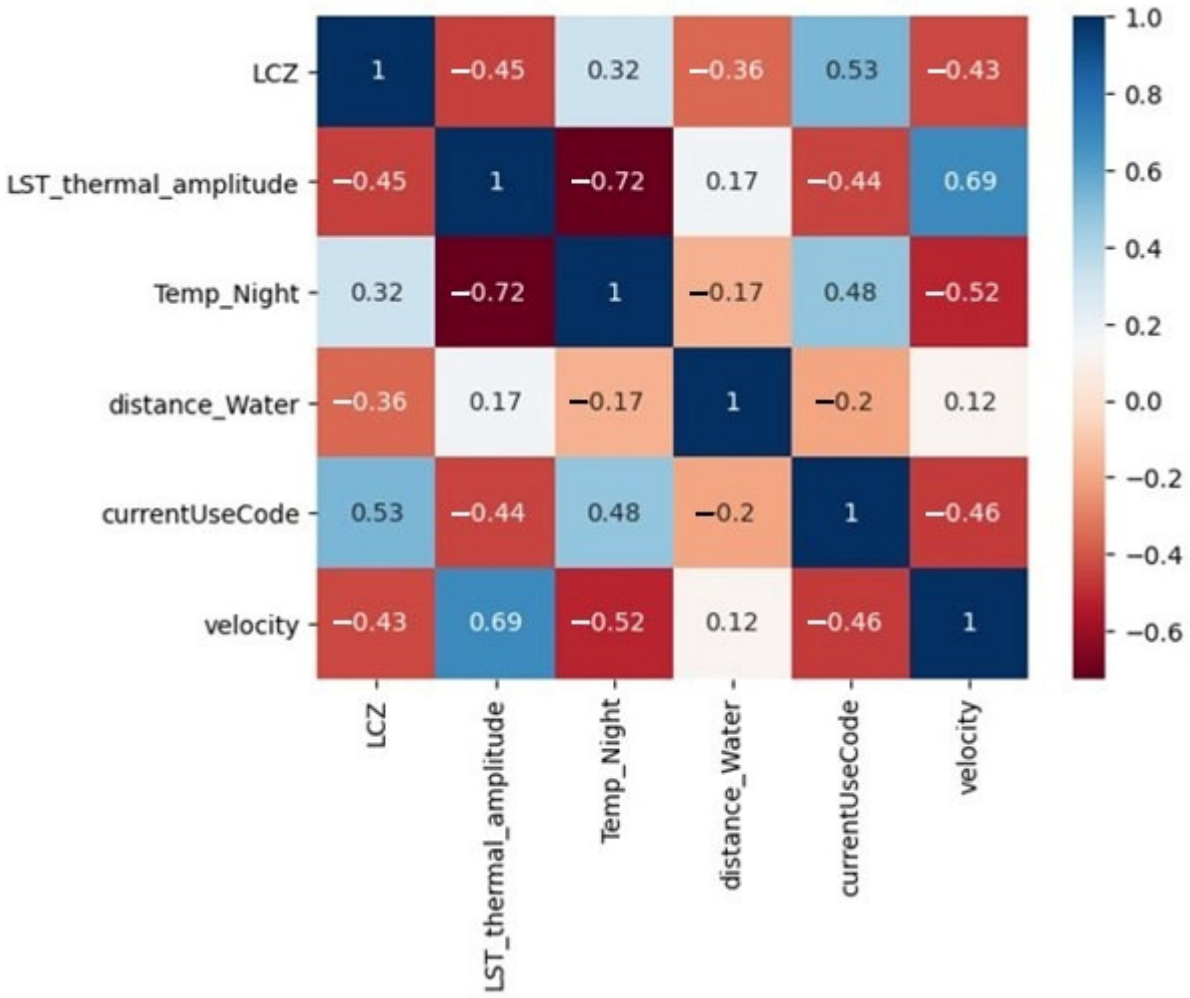

Figure 2. Correlation matrix, which displays the correlation coefficients between all possible pairs of variables in the dataset.

3.3. Bayesian Network Model

Two models were chosen in this study to anticipate potentially unstable zones in the study area: a Bayesian Network (BN) and a Multiple Linear Regression. The dependent variable for both models was the ground motion velocity, while the explanatory variables were the Local Climate Zones (LCZs), the Current Use Code of buildings and their distance to water, the nighttime land surface temperature (LST), and the temperature difference between day and night.

Bayesian Networks are probabilistic graphical models that use Directed Acyclic Graphs (DAG) to model the dependencies between variables. The DAG is constituted by nodes that represent the random variables and arches that join the different nodes defining the dependence structure. This dependence structure is defined using the one-parameter conditional copula [58], which defines the joint distribution of the two random variables. In this work, a Gaussian copula-based BN was employed. This type of BN has the advantage of being a hybrid BN [59] and can overcome large or complex problems due to its fast computation. The Gaussian copula-based BN defines the bivariate pieces of dependence using the product–moment correlation (ρ) [60]. This one is related to the rank correlation using Pearson's transformation, as stated in Equation (1) [61].

$$\rho(X, Y) = 2\,sin\left(\frac{\pi}{6} \cdot r(X, Y)\right) \quad (1)$$

In the particular case of the normal copulas, the joint normal distribution which builds the Bayesian Network uses the conditional correlations which are equivalent to the partial correlations. The arches which join the parent node with the child nodes are related with the conditional rank correlation following the DAG structure, as stated in Equation (2) [62].

$$\begin{cases} r\left(X_i,\ Pa_j(X_i)\right), & j = 1 \\ r\left(X_i,\ Pa_j(X_i) \middle| Pa_1(X_i), \ldots, Pa_{j-1}(X_i)\right), & j = 2, \ldots, m \end{cases} \tag{2}$$

where m is the number of parents $Pa_j(X_i)$ of the node X_i, and j is the node parent order. The joint distribution of n variables is computed by the BN following Equation (3) [63].

$$f_{1,\ldots,n}(x_1, \ldots, x_n) = f_1(x_1) \prod_{i=2}^{n} f_{i|Pa(i)}\left(x_i \middle| x_{Pa(i)}\right) \tag{3}$$

The Gaussian copula-based Bayesian Network employed in this work was implemented in BANSHEE, an open-access toolbox developed in MATLAB [64] and Python [65]. As the first step to building the BN, the correlation matrix is computed in the previous section (see Figure 2). The results obtained assist in the realization of the DAG design. Due to the nature of the model to be developed, and since the purpose was to use different variables (LCZ, LST Amplitude, Night Temperature, Distance Water, and Current Use Code) for velocity prediction, velocity was selected as the child node to the rest of the parameters. Following the results obtained in the correlation matrix, variables with correlations greater (in absolute terms) than 0.15 were joined by means of arcs. Variables with correlations lower than this value were considered independent. The DAG obtained for the Bayesian Network is shown in Figure 3. Following this DAG structure and the conditional rank correlation values computed by BANSHEE, the final correlation matrix was obtained. This correlation matrix defines the Bayesian Network, and its values can be observed in Figure 4.

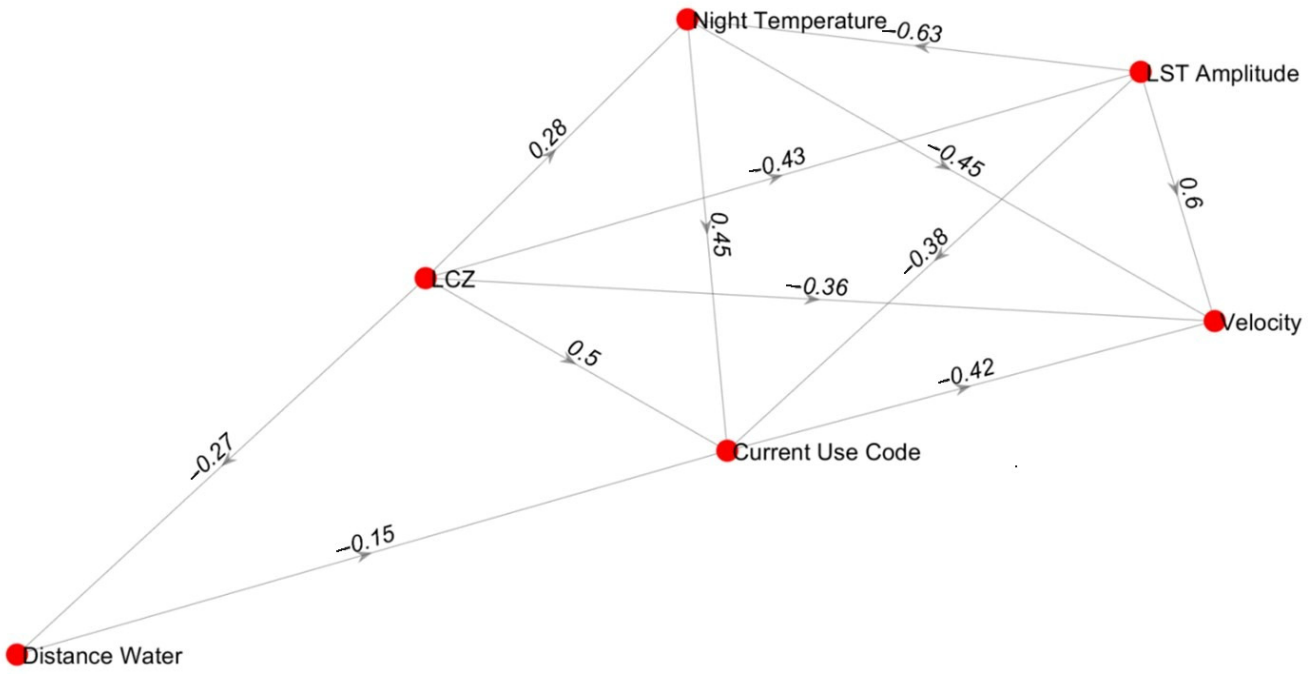

Figure 3. Designed DAG of the Bayesian Network with the conditional rank correlation values.

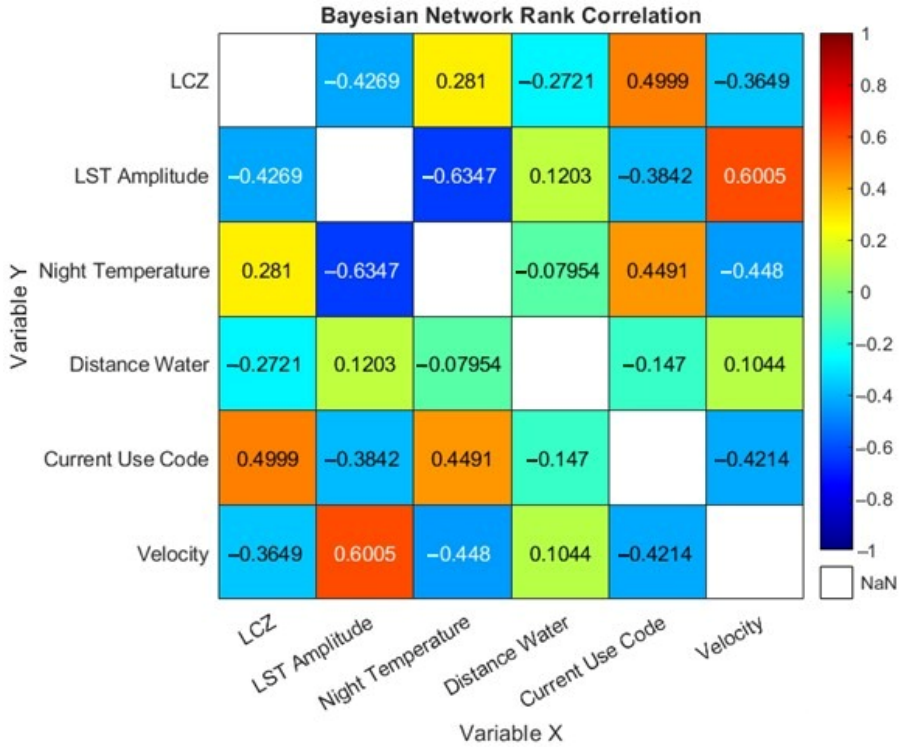

Figure 4. Correlation matrix computed using the BANSHEE toolbox for DAG employed to create the Bayesian Network.

3.4. Multiple Linear Regression Model

A Multiple Linear Regression (MLR) model is used to compare the prediction results of the BN. MLR is a statistical technique commonly used in scientific research to analyze the relationship between several variables. The same variables used in the BN model were used in the MLR model.

The MLR model assumes a linear relationship between the dependent variable and the independent variables, which means that the change in the dependent variable is proportional to the change in the independent variable. The MLR model creates a linear equation that best fits the data, with the aim of minimizing the difference between predicted and actual values.

To determine the values of the coefficients, the MLR model uses a method called Ordinary Least Squares (OLS), which finds the values of the coefficients that minimize the sum of the squared differences between predicted and actual values. This process is commonly known as "fitting" the model to the data.

Due to the nature of our data and to ensure that each variable was on the same scale, the data for each variable were transformed using a method called MinMaxScaler, which scales each feature to a specified range (default and in our case, between 0 and 1).

The linear equation takes the form: $y = b_0 + b_1x_1 + b_2x_2 + \ldots + b_nx_n$, where y is the dependent variable, b_0 is the intercept or constant term, b_1–b_n are the coefficients representing the effect of each independent variable on the dependent variable, and x_1–x_n are the independent variables.

To implement the MLR model, the Python package sklearn.linear was used, which provides tools for statistical data analysis, including multiple linear regression. The model was fitted to the training data, and its performance was then evaluated using various evaluation metrics such as Mean Absolute Error (MAE) and the coefficient of determination (R^2). These metrics are used to measure the accuracy and quality of the predictive model, respectively.

4. Results

4.1. Urban Monitoring Results

The Night Temperature (Nighttime LST) for the date of 28 August 2015 was obtained by processing Landsat-8 images, which was the only available data for our study area. Additionally, the temperature difference with respect to the daytime (LST Amplitude) was calculated by combining the images on 28 August 2015 and 3 August 2015, allowing the observation of urban heat island patterns. Comparing the land cover class of the European LCZ with the two thermal maps calculated for the study of nighttime LST, it is clear that there is a geographical correspondence between urban soils and "hotter" LST. This reveals the existence of the "nocturnal urban heat island" (NUHI) phenomenon, as shown in Figure 5, where the highest LST values match with urban soil and the lowest LST values appear on natural soil.

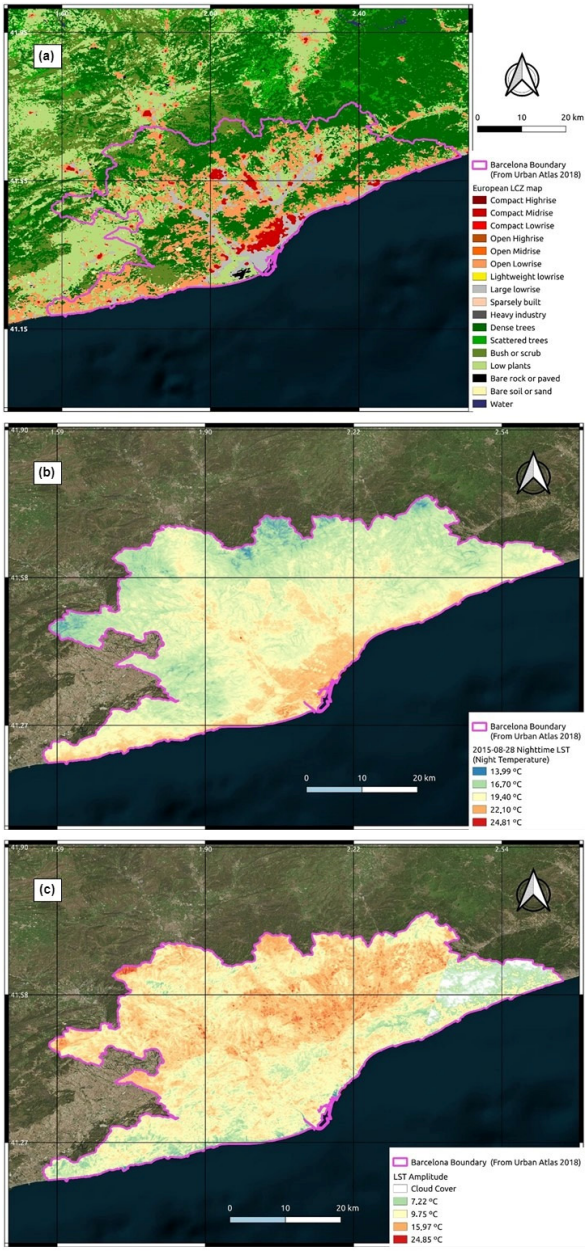

Figure 5. (**a**) Land cover according to the European LCZ map [52]; (**b**) Nighttime LST of the image capture dated 28 August 2015; (**c**) difference in daytime LST between the images on 3 August 2015 and 28 August 2015 with respect to the Nighttime LST of the image on 28 August 2015.

Ground temperature amplitude records from meteorological stations (existing in the study area and dated 28 August 2015) were contrasted against data (surrounding within 100 m of these stations) of land surface temperature (LST) amplitude. This comparison serves to support the findings related to the "nocturnal urban heat island" (NUHI) derived from the remote sensing data, revealing in Figure 6 consistent trends between the satellite-derived information and the temperature records from the meteorological stations, except for Monistrol de Montserrat.

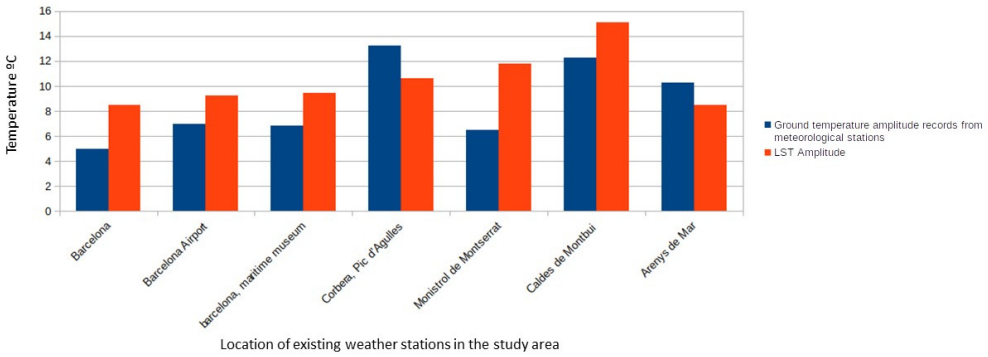

Figure 6. Ground-based amplitude temperature recordings from meteorological stations to verify the remote-sensing-derived LST Amplitude data.

To assess the risk of ground stability for the infrastructure in the study area, a ground motion velocity line of sight (LOS) map in descending geometry was obtained and is shown in Figure 7. As can be seen, almost all the infrastructure in the study area remains stable, with some unstable zones above a velocity ± 2 mm/year, mainly concentrated in the port and airport areas.

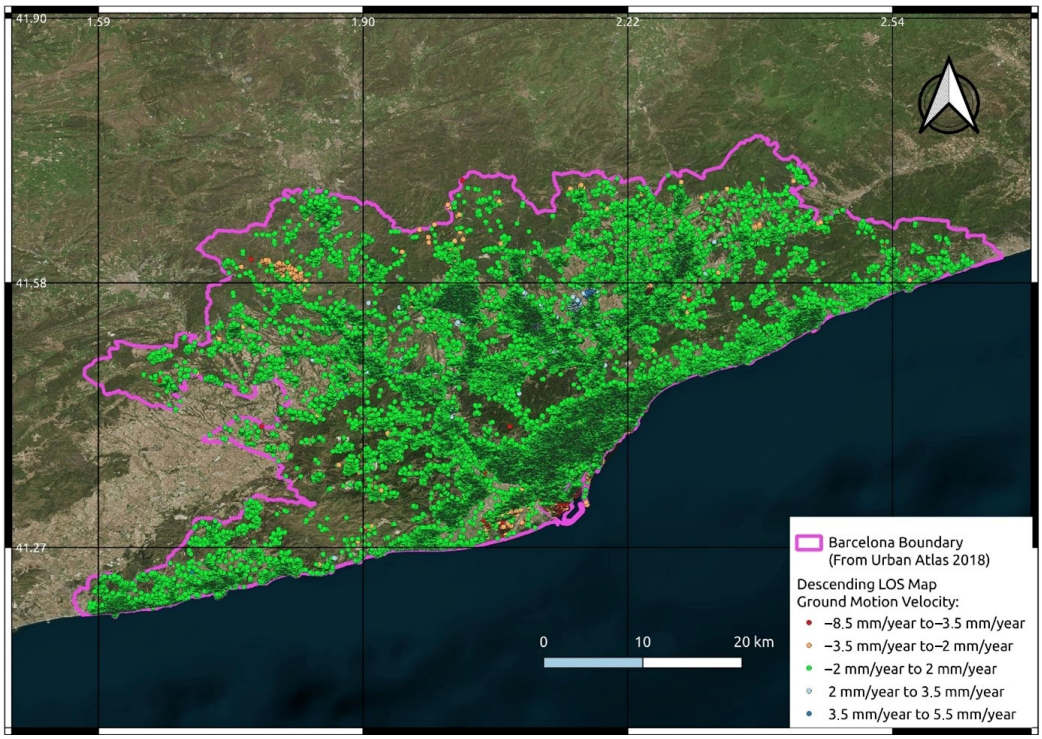

Figure 7. Ground motion velocity line of sight (LOS) map in descending geometry in the study area. The points with ±2 mm/year of velocity are considered stable points.

Since there are more stable points than unstable ones in the study area, data resampling was necessary to obtain a balanced distribution for correlation analysis and subsequent

prediction. In our case, we performed an undersampling of stable points to balance the number of stable and unstable points (obtaining 569 for stable and 551 for unstable). The undersampled points were selected by proximity (nearest neighbor) to the unstable points located only in the urban infrastructures, excluding the ground motion information points located in nonconstructed areas such as forests, crops, or water bodies. This provided a distributed representation throughout the study area, allowing for a better understanding of the relationships between ground motion velocity and other variables. The velocity LOS map of the resampled data for correlation analysis and subsequent prediction is depicted in Figure 8.

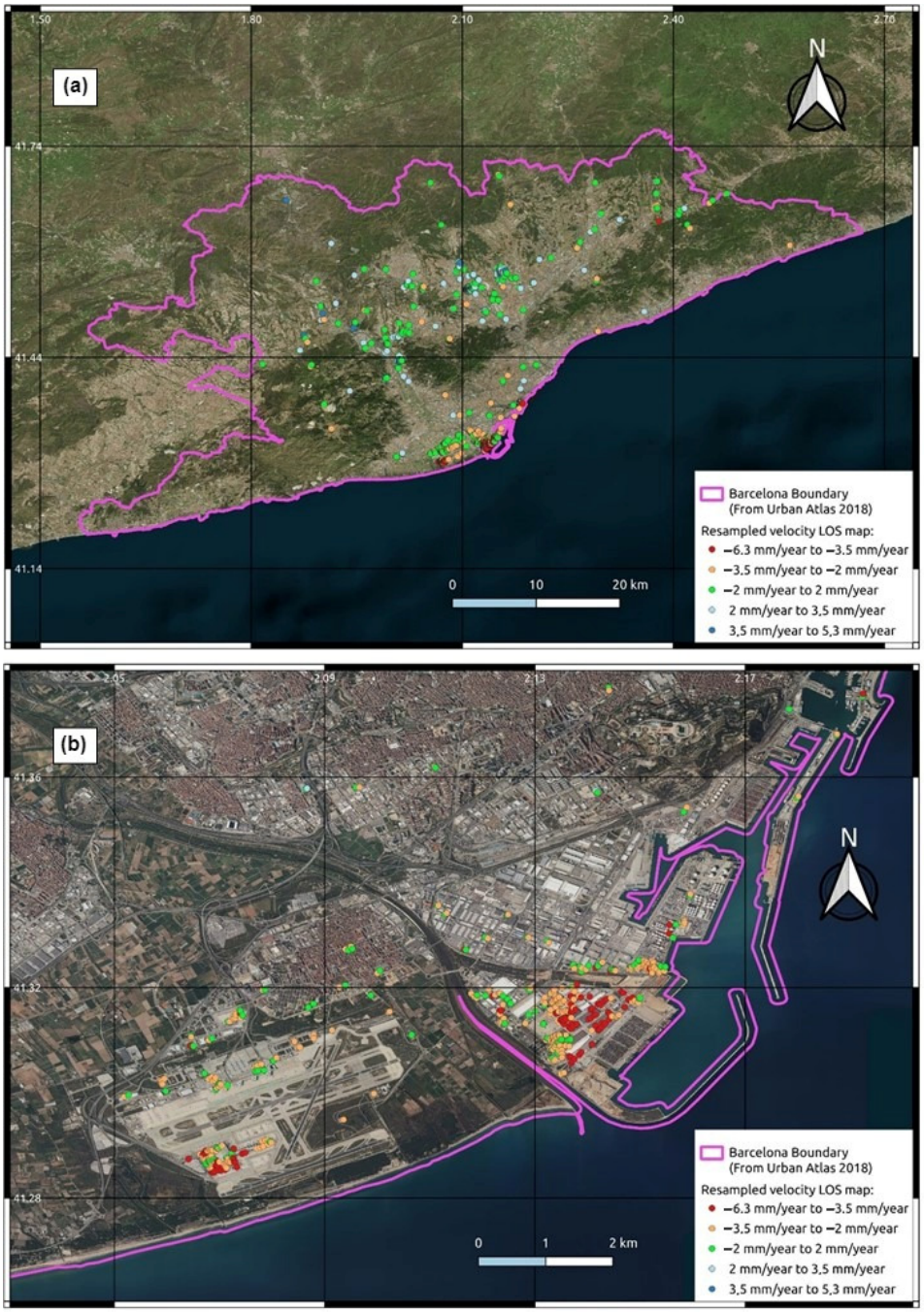

Figure 8. (**a**) Resampled velocity LOS map of the points of information only located in the urban infrastructures; (**b**) detail of the Barcelona port and airport area on the resampled velocity LOS map.

Figure 9 shows the Current Use Code and the distance from the infrastructures to water bodies that geographically coincide with the resampled points of ground motion velocity.

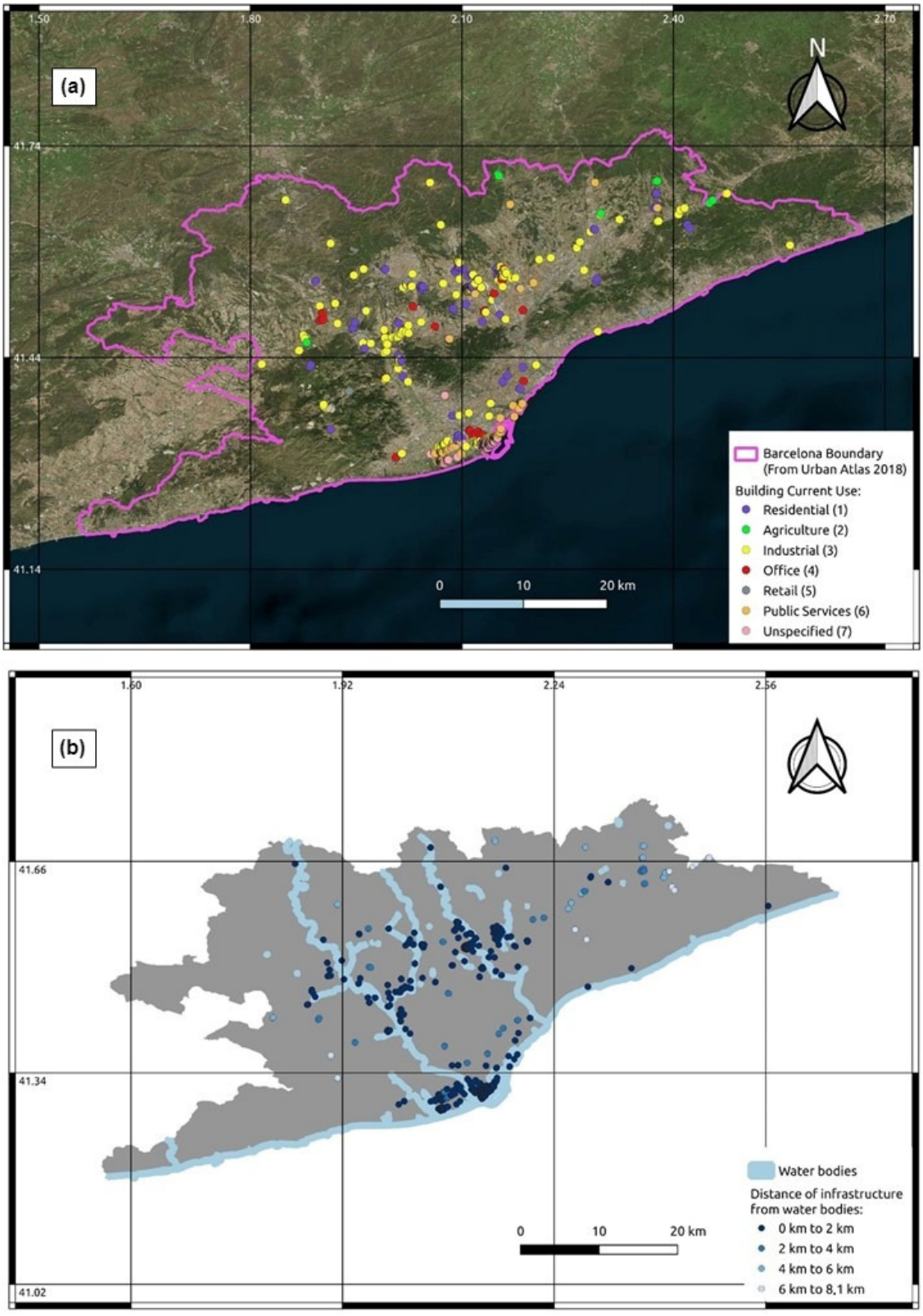

Figure 9. (**a**) The Current Use Code of the infrastructures at the resampled points for ground motion velocity; (**b**) distance to water bodies of the infrastructures.

4.2. Relationship among Variables

The correlation coefficients among all possible variable combinations in the dataset were analyzed (Figure 2). The LST Amplitude and Night Temperature variables had the strongest correlation, but this was due to its causal relationship, since LST Amplitude is the difference between Night Temperature and Daytime Temperature values. Thus, the ground motion velocity is the variable that best relates to the other variables studied.

The velocity variable is moderately related to the two variables that describe the "nocturnal urban heat island" (NUHI) effect, namely LST Amplitude and Night Temperature. Because the velocity variable, which describes the ground stability of infrastructures, may have an additional connection to the health risks for the inhabitants of the study area due to climate change, this could indicate urban inequalities in certain areas of the territory due to the lack of consideration of such risks in urban planning.

Therefore, velocity is considered the most important variable to predict, as it indicates the future risk ground stability of the city. Additionally, choosing velocity as the variable to predict has the advantage of getting data quickly and easily, without the need for Mt-InSAR processing, which is time-consuming and computationally expensive.

Variables describing soil characteristics and distance to water bodies are included as an exploratory analysis in the identification of unexpected patterns or relationships between unrelated variables and the target variable in order to reveal possible complex interactions or indirect effects that justify their inclusion in the model. This decision is motivated by the fact that the intrinsic nature of soil characteristics affects soil stability and that distance to water bodies is an important factor in the analysis of potential risks in the event of a climatic emergency.

4.3. Model Results

The Bayesian Network model was constructed based on the correlation values obtained by the BANSHEE toolbox, and training was performed with 80% of the resampling data. The remaining 20% of the data were used for prediction and for the subsequent comparison with the multiple regression model used to validate the methodology.

One of the advantages of this model is the ability to generate a large amount of data for each prediction. In our case, 10,000 synthetic data were generated for each of the 225 expected predictions. Figure 10 shows three examples of velocity predictions generated using the Bayesian Network model: one with a good prediction value, another with an acceptable value, and one with a bad prediction value.

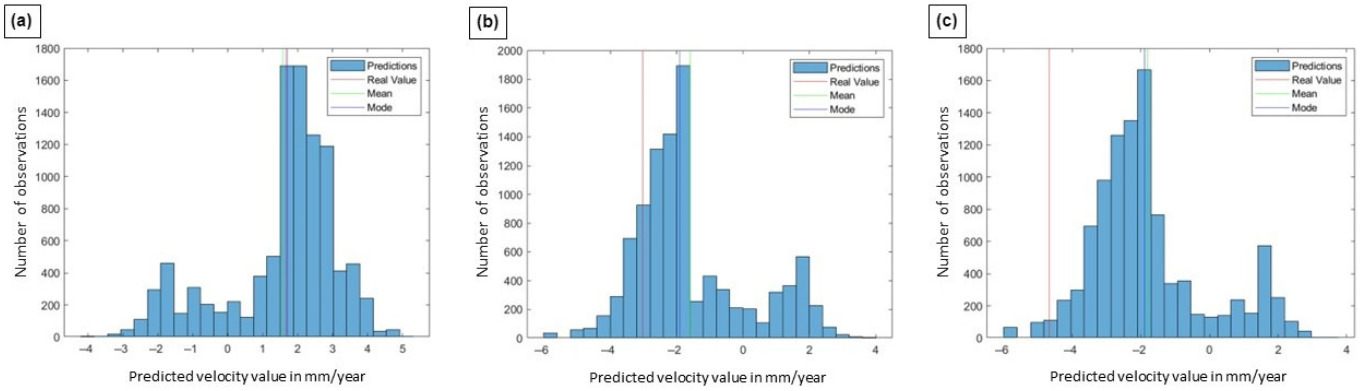

Figure 10. Histograms that represent the predicted velocity value by the Bayesian Network model (with intervals of 0.2 mm/year). The red line indicates the actual velocity for a specific point. The three subfigures (**a**–**c**) represent the cases of good, acceptable, and bad predictions, respectively, considering the mean and mode values of the predictions.

In some cases, the generated data resulted in bimodal distributions, as depicted in Figure 11, which made it necessary to use the mode of the generated data distribution as the most probable prediction value instead of the mean value, as it better represents the results. However, some predictions tend to the second mode, making it difficult to ensure their accuracy.

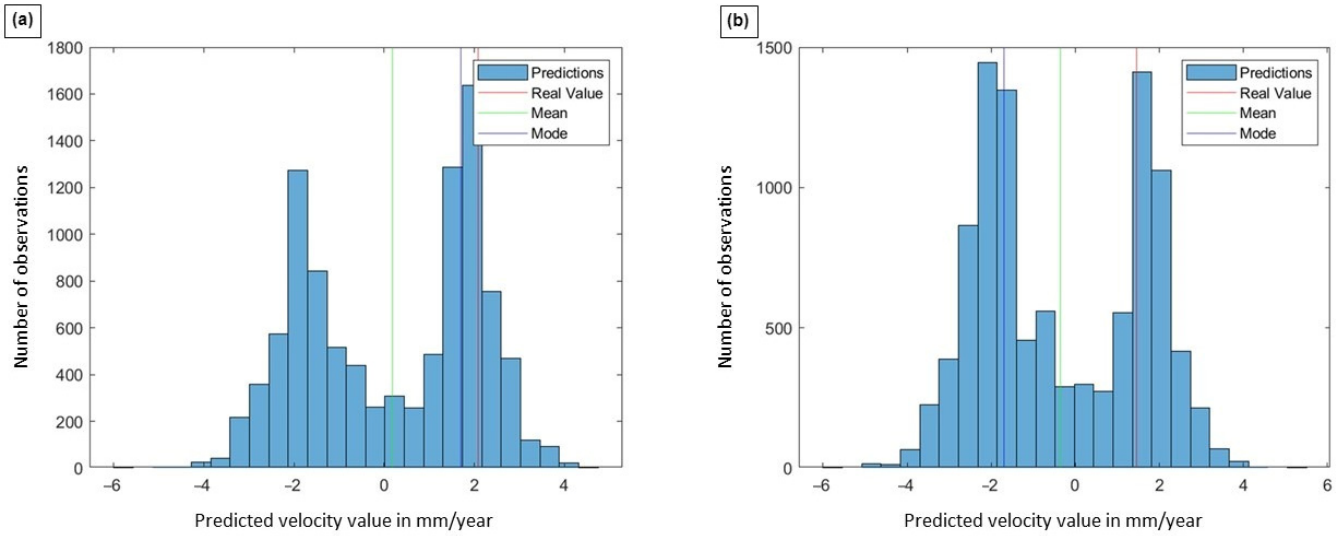

Figure 11. (**a**) Bimodal distribution with a correct prediction as the true value coincides with the main mode; (**b**) bimodal distribution with an incorrect prediction as the true predicted value tends to the second mode.

In this context, it is essential to highlight that the present model is focused on the generation of estimates related to ground motion, based on numerical parameters that can be acquired by any urban manager. These parameters, namely LCZ, LST Amplitude, Night Temperature, Distance Water, and Current Use Code, prove to be more intuitive options as opposed to the inclusion of specific geospatial coordinates. It is worth mentioning that the use of specific coordinates would allow the model to geolocate and represent risk areas on a map, resulting in a more targeted approach. However, our model makes it possible to make decisions related to urban infrastructure stability in an anticipatory and accessible manner by employing global data and features. This, in turn, provides the ability to interpret ground motion values that can be identified as risk areas, contributing to the mitigation of urban inequalities in the face of climate change risks.

4.4. Model Validation

To address this uncertainty, we adapted two validation metrics to help determine the accuracy of the model results. As the predictions of the Bayesian Network model are a set of velocity values (in this work set to 10,000 samples), it is not possible to compare them with a single experimental velocity result.

Two validation methods shown in Table 1 were employed to check the robustness of the Bayesian Network model. The first one compares the experimental result with a mode interval (defined for bins of 0.2 mm/year). The second one compares the experimental result with the mean value obtained in the distribution supplied by the Bayesian Network. The success rate of each validation method was defined considering different maximum velocity errors (0.5, 1.0, 1.5, 2 mm/year). The success rate would be the number of predictions with a velocity difference (regarding the experimental result) lower than the maximum error considered.

Table 1. Success rate of the predictions of the Bayesian Network considering maximum error for each validation method.

Validation Method	Maximum Error ± 0.5 mm/Year	Maximum Error ± 1.0 mm/Year	Maximum Error ± 1.5 mm/Year	Maximum Error ± 2.0 mm/Year
Mode Interval	43.00%	65.00%	81.00%	88.00%
Mean value	23.00%	46.00%	65.00%	80.00%

A comparison with another model widely used in the scientific community, the Mean Absolute Error (MAE), regarding the mean and mode interval (using a bin width of 0.2mm/year) and the coefficient of determination (R^2) was computed. Table 2 summarizes the results of the adapted performance metrics.

Table 2. Bayesian Network model validation metrics.

Bayesian Network Model	
MAE with respect to mean	1.24
MAE with respect to mode	0.92
R^2	0.60

New velocity predictions are performed with the multiple regression model, and the evaluation metrics of MAE and R^2 are obtained. Table 3 summarizes the results of the performance metrics of the multiple regression model. In this way, the goodness of fit of the Bayesian Network model results is compared.

Table 3. Multiple Linear Regression model validation metrics.

Multiple Linear Regression Model	
MAE	1.14
R^2	0.61

The use of these metrics provides insight into the pros and cons of using the Bayesian Network model as an urban planning tool in terms of predictive accuracy and model quality.

As observed in Tables 2 and 3, both models achieved similar results. Due to the limited amount of data (resampled data due to the scarcity of unstable velocity data) and the obtained correlations, it is challenging to obtain more reliable results.

Nevertheless, the results are considered acceptable in view of the limited effort needed to obtain ground motion velocities, without depending on the Mt-InSAR technique. This is one of the most relevant advantages of this study. Additionally, the use of the Bayesian Network model has the advantage over the multiple regression analysis of being capable of representing the model's uncertainty by generating a large number of synthetic data through probability distributions.

5. Discussion

In our work, nocturnal urban heat island (NUHI) patterns were detected in the selected study area, which are consistent with those obtained for the Metropolitan Area of Barcelona (MAB) [18,48]. Thus, our approach is validated. This work improves the aforementioned work, as well as other studies, because it only analyzes land surface temperature (LST) as an indicator of climatic risk in cities [16,17,19,66]. In our approach, we add information on risk urban infrastructures in terms of ground motion, achieving a richer analysis. Additionally, we found synergies of different types of satellite imagery to assess the urban risks, detecting some unstable areas in our analysis assessing climate change-related risk areas. These zones are the port of Barcelona and the airport area, which fit the results of previous works [49], so the quality of the results obtained with Mt-InSAR are demonstrated.

The possible causes of the deformation could be, for example, attributed to water pumping activities, while those in other areas stem from construction activities or, for example, associated with land reclamation efforts, such as the protective dikes surrounding the port [49]. It is crucial to consider these factors in future research, as they can potentially impact the effectiveness of the proposed model. One approach could involve incorporating a new layer of geographic information that categorizes soil based on these factors. For instance, including variables like "water pumping activities" (Yes or No), "recent construction activities" (Yes or No), etc., could yield more informative results. This would likely lead to a more accurate and robust model overall.

As for studies that combine radar and multispectral images [32–36], they have only focused their efforts on a causal analysis between both types of images, with very few studies taking a holistic approach to finding hidden relationships between both types of information. In this sense, only one work was found using this approach [37]. Our work continues this approach and goes further by including water risk factors and the construction of a Bayesian Network capable of generating synthetic data that will help future decision making, serving as another urban design tool.

The results of Mt-InSAR identify buildings that may require further on-site investigation, thereby strengthening preventive measures within the urban management process. In this way, intervention measures that can be taken (for example, establishing new areas of vegetation, expanding existing ones, or eliminating risk infrastructures) would be more effective when using information related to the location of heat islands and the risk of infrastructures due to their extreme ground motion values.

Even though urban remote sensing is a well-developed subdomain in remote sensing science, the degree to which remote sensing is used in the science of urban ecological planning and the way it contributes to urban policy remain unclear [12]. Our work represents one more example of how remote sensing technologies allow large-scale analysis and monitoring of the territory over time, including the analysis of the past and present and using predictive modeling for projections into the future. The results of our study strengthen that combining remote sensing with predictive modeling can assist decision making and policy development related to urban planning and climate change adaptation. Therefore, this work improves the understanding of the risk of cities to the climate emergency by combining diverse inputs, being one of the first studies to associate nocturnal LST and ground motion through Landsat-8 and Sentinel-1 images. To that end, two predictive approaches, namely a Bayesian Network and Multiple Linear Regression, were built to anticipate urban risks in the study area.

The performance of the BN model was compared with the MLR model using similar evaluation metrics, and it was found that the BN model matched the MLR model in predicting the values of the velocity variable. Despite the lack of strong correlations between the variables analyzed, the BN model is still able to generate synthetic data by means of distributions and can represent their uncertainty, which is its greatest advantage. These results demonstrate that the BN model is an effective and appropriate technique for modeling and predicting complex datasets.

Overall, the results of this study demonstrate the potential of satellite remote sensing to inform urban planning and climate change adaptation strategies. By providing detailed information on risk areas and infrastructure, satellite data can help decision-makers anticipate and respond to emerging risks and develop effective interventions that can protect cities and their inhabitants from the impacts of climate change. Future research in this area should continue to explore the potential of high-resolution satellite data (ASTER, Sentinel-2, KOMPSAT, TerraSAR-X, COSMO-SkyMed, or PAZ) or through the use of machine learning algorithms to improve the resolution of medium-resolution images.

6. Conclusions

The main objective of this research was achieved by showing the relationships that exist between (i) Local Climate Zones, (ii) the current land use where the infrastructure

asset is placed, (iii) the distance from this asset to water bodies, (iv) the NUHI through the nocturnal LST that exists in the study area, and (v) the ground motion. These variables were taken into account to identify both risk areas of ground stability and climate-change-related risk areas.

After analyzing the results, we can extract the following conclusions. The study uses free, multispectral satellite images (through the NASA/USGS Landsat program) and radar images (through the European Union Earth Observation Program, Copernicus), as well as the European LCZ map (available on the WUDAPT data portal) and the current use of existing buildings in the study area of Barcelona (through the INSPIRE service of cadastral mapping). This allows the development of urban planning and management instruments to equip city authorities and managers with the necessary decision-making tools to effectively address the current climate emergency and mitigate potential issues in urban infrastructures. This, in turn, can significantly improve the quality of life for citizens by reducing risk and inequalities within the city.

This study represents a pioneering effort to identify areas that are particularly unsuitable for public health during the hottest nights caused by the urban heat island phenomenon resulting from global warming. The approach involves analyzing nighttime land surface temperature (LST) and linking it to the location of unstable infrastructure using the Mt-InSAR (Multitemporal Interferometric Synthetic Aperture Radar) technique, which is capable of detecting the speed of Earth's surface displacement. The expectation of this research is to enhance city resilience by exploring strategies for modifying land cover and land use to create safer and more sustainable cities.

The development of a Bayesian Network model represents a key step in equipping urban planning authorities with the means to deal with climate change. This model uses multispectral satellite and radar images, leveraging the power of probabilistic graphical models to account for model uncertainties. Comparison with the Multiple Linear Regression model, a reliable technique for predicting complex relationships, confirmed the effectiveness of our approach as a tool for predicting ground motion in urban infrastructures in order to localize the risk areas of ground stability in the study area or, in other words, to localize areas with urban inequalities due to global climate change through the new approach of resilient urbanism: one resilient urbanism focused not on solving problems but on anticipating them [67].

Author Contributions: Conceptualization, B.R. and J.M.-S.; methodology, I.R.-A. and B.B.; software, I.R.-A. and B.B.; validation, I.R.-A. and B.B.; formal analysis, B.R. and J.M.-S.; investigation, all; resources, I.R.-A. and B.B.; writing—original draft preparation, I.R.-A. and B.B.; writing—review and editing, B.R. and J.M.-S.; supervision, J.M.-S. and B.R.; project administration, J.M.-S.; funding acquisition, B.R. All authors have read and agreed to the published version of the manuscript.

Funding: This work has been funded by the Spanish Ministry of Science and Innovation through the PONT3 project Ref. PID2021-124236OB-C33 and through the grant PRE2019-087331 for the training of predoctoral researchers.

Data Availability Statement: The data that support the findings of this study are available from various open-access sources. The Landsat-8 and Sentinel-1 satellite data were obtained from the USGS National Land Imaging (NLI) Program and The Copernicus Open Access Hub, respectively. The land cover and land use datasets were sourced from the official WUDAPT data portal and the INSPIRE Cadastre Cartography QGIS plugin, respectively.

Conflicts of Interest: The authors declare no conflicts of interest.

References

1. Chmutina, K.; Ganor, T.; Bosher, L. Role of urban design and planning in disaster risk reduction. *Proc. Inst. Civ. Eng.-Urban Des. Plan.* **2015**, *167*, 125–135. [CrossRef]
2. Xing, Z.; Yang, S.; Zan, X.; Dong, X.; Yao, Y.; Liu, Z.; Zhang, X. Flood vulnerability assessment of urban buildings based on integrating high-resolution remote sensing and street view images. *Sustain. Cities Soc.* **2023**, *92*, 104467. [CrossRef]

3. Yu, S.; Yuan, M.; Wang, Q.; Corcoran, J.; Xu, Z.; Peng, J. Dealing with urban floods within a resilience framework regarding disaster stages. *Habitat. Int.* **2023**, *136*, 102783. [CrossRef]
4. Antuñano, I.R. Repensar el urbanismo como solución al cambio climático: Caso de estudio: Área Metropolitana Asturiana. In Proceedings of the IV Congreso ISUF-H: Metrópolis en Recomposición: Prospectivas Proyectuales en el Siglo XXI: Forma Urbis y Territorios Metropolitanos, Barcelona, Spain, 28–30 September 2020; pp. 1–22. Available online: https://upcommons.upc.edu/handle/2117/328891 (accessed on 1 June 2024).
5. You, M.; Huang, J.; Guan, C.H. Are New Towns Prone to Urban Heat Island Effect? Implications for Planning Form and Function. *Sustain. Cities Soc.* **2023**, *99*, 104939. [CrossRef]
6. Sofina, N.; Ehlers, M. Building Change Detection Using High Resolution Remotely Sensed Data and GIS. *IEEE J. Sel. Top. Appl. Earth Obs. Remote Sens.* **2016**, *9*, 3430–3438. [CrossRef]
7. Agarwal, V.; Kumar, A.; Qin, Z.; Gomes, R.L.; Marsh, S. Lessons for Sustainable Urban Development: Interplay of Construction, Groundwater Withdrawal, and Land Subsidence at Battersea, London. *Remote Sens.* **2023**, *15*, 3798. [CrossRef]
8. Rodríguez-Antuñano, I.; Martínez-Sánchez, J.; Cabaleiro, M.; Riveiro, B. Anticipating the Collapse of Urban Infrastructure: A Methodology Based on Earth Observation and MT-InSAR. *Remote Sens.* **2023**, *15*, 3867. [CrossRef]
9. Rodríguez-Antuñano, I.; Martínez-Sánchez, J.; Lagüela-López, S.; Riveiro, B. Towards more resilient smart cities: Mt-insar monitoring of urban infrastructure using machine learning techniques. *ISPRS Ann. Photogramm. Remote Sens. Spat. Inf. Sci.* **2022**, *X-4-W3-2022*, 221–228. [CrossRef]
10. Zhou, L.; Zhang, X.; Shen, H.; Zhang, D.; Bao, H. GIS analysis of urban ground collapse susceptibility: A case study of eastern Hangzhou, China. *Front. Earth Sci.* **2023**, *11*, 1338877. [CrossRef]
11. UN-HABITAT. Resilience and Risk Reduction | UN-Habitat. Available online: https://unhabitat.org/topic/resilience-and-risk-reduction (accessed on 29 March 2023).
12. Wellmann, T.; Lausch, A.; Andersson, E.; Knapp, S.; Cortinovis, C.; Jache, J.; Scheuer, S.; Kremer, P.; Mascarenhas, A.; Kraemer, R.; et al. Remote sensing in urban planning: Contributions towards ecologically sound policies? *Landsc. Urban Plan.* **2020**, *204*, 103921. [CrossRef]
13. Tortini, R.; Mayer, A.L.; Hermosilla, T.; Coops, N.C.; Wulder, M.A. Using annual Landsat imagery to identify harvesting over a range of intensities for non-industrial family forests. *Landsc. Urban Plan.* **2019**, *188*, 143–150. [CrossRef]
14. Oke, T.R. City size and the urban heat island. *Atmos. Environ. (1967)* **1973**, *7*, 769–779. [CrossRef]
15. Tan, J.; Zheng, Y.; Tang, X.; Guo, C.; Li, L.; Song, G.; Zhen, X.; Yuan, D.; Kalkstein, A.J.; Li, F.; et al. The urban heat island and its impact on heat waves and human health in Shanghai. *Int. J. Biometeorol.* **2010**, *54*, 75–84. [CrossRef] [PubMed]
16. Liu, L.; Zhang, Y. Urban Heat Island Analysis Using the Landsat TM Data and ASTER Data: A Case Study in Hong Kong. *Remote Sens.* **2011**, *3*, 1535–1552. [CrossRef]
17. Yao, Y.; Chang, C.; Ndayisaba, F.; Wang, S. A new approach for surface urban heat island monitoring based on machine learning algorithm and spatiotemporal fusion model. *IEEE Access* **2020**, *8*, 164268–164281. [CrossRef]
18. Arellano, B.; Roca, J. Remote Sensing and Night Time Urban Heat Island. *Int. Arch. Photogramm. Remote Sens. Spat. Inf. Sci.* **2021**, *XLIII-B3-2021*, 15–22. [CrossRef]
19. Siddiqui, A.; Kushwaha, G.; Nikam, B.; Srivastav, S.K.; Shelar, A.; Kumar, P. Analysing the day/night seasonal and annual changes and trends in land surface temperature and surface urban heat island intensity (SUHII) for Indian cities. *Sustain. Cities Soc.* **2021**, *75*, 103374. [CrossRef]
20. Zebker, H.; Shankar, P.; Hooper, A. InSAR remote sensing over decorrelating terrains: Persistent scattering methods. In Proceedings of the 2007 IEEE Radar Conference, Waltham, MA, USA, 17–20 April 2007; pp. 717–722. [CrossRef]
21. Daout, S.; Doin, M.P.; Peltzer, G.; Socquet, A.; Lasserre, C. Large-scale InSAR monitoring of permafrost freeze-thaw cycles on the Tibetan Plateau. *Geophys. Res. Lett.* **2017**, *44*, 901–909. [CrossRef]
22. Cha, A.; Kim, T.H. Relationship Of Debris Flows Owing To Climate Change: Korea's Case. *WIT Trans. Built Environ.* **2013**, *133*, 57–66. [CrossRef]
23. Bakon, M.; Perissin, D.; Lazecky, M.; Papco, J. Infrastructure Non-linear Deformation Monitoring Via Satellite Radar Interferometry. *Procedia Technol.* **2014**, *16*, 294–300. [CrossRef]
24. Sousa, J.J.; Bastos, L. Multi-temporal SAR interferometry reveals acceleration of bridge sinking before collapse. *Nat. Hazards Earth Syst. Sci.* **2013**, *13*, 659–667. [CrossRef]
25. Handwerger, A.L.; Huang, M.H.; Fielding, E.J.; Booth, A.M.; Bürgmann, R. A shift from drought to extreme rainfall drives a stable landslide to catastrophic failure. *Sci. Rep.* **2019**, *9*, 1569. [CrossRef] [PubMed]
26. Huong, D.T.V.; Nagasawa, R. Potential flood hazard assessment by integration of ALOS PALSAR and ASTER GDEM: A case study for the Hoa Chau commune, Hoa Vang district, in central Vietnam. *J. Appl. Remote Sens.* **2014**, *8*, 083626. [CrossRef]
27. Li, Y.; Martinis, S.; Wieland, M. Urban flood mapping with an active self-learning convolutional neural network based on TerraSAR-X intensity and interferometric coherence. *ISPRS J. Photogramm. Remote Sens.* **2019**, *152*, 178–191. [CrossRef]
28. Zhao, J.; Li, Y.; Matgen, P.; Pelich, R.; Hostache, R.; Wagner, W.; Chini, M. Urban-Aware U-Net for Large-Scale Urban Flood Mapping Using Multitemporal Sentinel-1 Intensity and Interferometric Coherence. *IEEE Trans. Geosci. Remote Sens.* **2022**, *60*, 1–21. [CrossRef]
29. Wang, Y.; Chew, A.W.Z.; Zhang, L. Building damage detection from satellite images after natural disasters on extremely imbalanced datasets. *Autom. Constr.* **2022**, *140*, 104328. [CrossRef]

30. Chowdhuri, I.; Pal, S.C.; Chakrabortty, R. Flood susceptibility mapping by ensemble evidential belief function and binomial logistic regression model on river basin of eastern India. *Adv. Space Res.* **2020**, *65*, 1466–1489. [CrossRef]
31. Norallahi, M.; Kaboli, H.S. Urban flood hazard mapping using machine learning models: GARP, RF, MaxEnt and NB. *Nat. Hazards* **2021**, *106*, 119–137. [CrossRef]
32. Maltese, A.; Pipitone, C.; Dardanelli, G.; Capodici, F.; Muller, J.-P. Toward a Comprehensive Dam Monitoring: On-Site and Remote-Retrieved Forcing Factors and Resulting Displacements (GNSS and PS–InSAR). *Remote Sens.* **2021**, *13*, 1543. [CrossRef]
33. Mirzadeh, S.M.J.; Jin, S.; Parizi, E.; Chaussard, E.; Bürgmann, R.; Blasco, J.M.D.; Amani, M.; Bao, H.; Mirzadeh, S.H. Characterization of Irreversible Land Subsidence in the Yazd-Ardakan Plain, Iran From 2003 to 2020 InSAR Time Series. *J. Geophys. Res. Solid Earth* **2021**, *126*, e2021JB022258. [CrossRef]
34. Kim, J.; Lin, S.Y.; Singh, R.P.; Lan, C.W.; Yun, H.W. Underground burning of Jharia coal mine (India) and associated surface deformation using InSAR data. *Int. J. Appl. Earth Obs. Geoinf.* **2021**, *103*, 102524. [CrossRef]
35. Karanam, V.; Motagh, M.; Garg, S.; Jain, K. Multi-sensor remote sensing analysis of coal fire induced land subsidence in Jharia Coalfields, Jharkhand, India. *Int. J. Appl. Earth Obs. Geoinf.* **2021**, *102*, 102439. [CrossRef]
36. Zhang, P.; Chen, Y.; Chen, Y. Permafrost Stability and Land Surface Temperature Distribution Study Using Multi-Source Remote Sensing Data in the Qinghai-Tibet Plateau. *Int. Geosci. Remote Sens. Symp. (IGARSS)* **2022**, *2022*, 3915–3918. [CrossRef]
37. Moise, C.; Negula, I.D.; Mihalache, C.E.; Lazar, A.M.; Dedulescu, A.L.; Rustoiu, G.T.; Inel, I.C.; Badea, A. Remote Sensing for Cultural Heritage Assessment and Monitoring: The Case Study of Alba Iulia. *Sustainability* **2021**, *13*, 1406. [CrossRef]
38. Pearl, J. *Probabilistic Reasoning in Intelligent Systems: Networks of Plausible Inference-Judea Pearl-Google Libri*; Morgan Kaufmann: Burlington, MA, USA, 1988.
39. Sebastian, A.; Dupuits, E.J.C.; Morales-Nápoles, O. Applying a Bayesian network based on Gaussian copulas to model the hydraulic boundary conditions for hurricane flood risk analysis in a coastal watershed. *Coast. Eng.* **2017**, *125*, 42–50. [CrossRef]
40. Torres-Alves, G.A.; Morales-Nápoles, O. Reliability analysis of flood defenses: The case of the Nezahualcoyotl dike in the aztec city of Tenochtitlan. *Reliab. Eng. Syst. Saf.* **2020**, *203*, 107057. [CrossRef]
41. Wu, X.; Feng, Z.; Liu, Y.; Qin, Y.; Yang, T.; Duan, J. Enhanced safety prediction of vault settlement in urban tunnels using the pair-copula and Bayesian network. *Appl. Soft. Comput.* **2023**, *132*, 109711. [CrossRef]
42. Grêt-Regamey, A.; Straub, D. Spatially explicit avalanche risk assessment linking Bayesian networks to a GIS. *Hazards Earth Syst. Sci.* **2006**, *6*, 911–926. [CrossRef]
43. D'Addabbo, A.; Refice, A.; Pasquariello, G. A Bayesian network approach to perform SAR/InSAR data fusion in a flood detection problem. In Proceedings of the Image and Signal Processing for Remote Sensing XX, Amsterdam, The Netherlands, 22–25 September 2014; Volume 9244, pp. 353–363. [CrossRef]
44. Li, Y.; Martinis, S.; Wieland, M.; Schlaffer, S.; Natsuaki, R. Urban Flood Mapping Using SAR Intensity and Interferometric Coherence via Bayesian Network Fusion. *Remote Sens.* **2019**, *11*, 2231. [CrossRef]
45. Qin, D.; Jianwen, M.; Yun, O.Y. Remote sensing data change detection based on the CI test of Bayesian networks. *Comput. Geosci.* **2006**, *32*, 195–202. [CrossRef]
46. Bolouki, S.M.; Ramazi, H.R.; Maghsoudi, A.; Pour, A.B.; Sohrabi, G. A Remote Sensing-Based Application of Bayesian Networks for Epithermal Gold Potential Mapping in Ahar-Arasbaran Area, NW Iran. *Remote Sens.* **2020**, *12*, 105. [CrossRef]
47. Varma, K.; Srivastava, V.; Singhal, A.; Jha, P.K. Urban and Environmental Hazards. In *Recent Technologies for Disaster Management and Risk Reduction. Earth and Environmental Sciences Library*; Springer: Cham, Switzerland, 2021; pp. 319–362. [CrossRef]
48. Arellano, B.; Roca, J. Effects of Urban Greenery on Health: A Study from Remote Sensing. *Int. Arch. Photogramm. Remote Sens. Spat. Inf. Sci.* **2022**, *43*, 17–24. [CrossRef]
49. Crosetto, M.; Solari, L.; Barra, A.; Monserrat, O.; Cuevas-González, M.; Palamà, R.; Wassie, Y.; Shahbazi, S.; Mirmazloumi, S.M.; Crippa, B.; et al. Analysis of the products of the copernicus ground motion service. *Int. Arch. Photogramm. Remote Sens. Spat. Inf. Sci.* **2022**, *43*, 257–262. [CrossRef]
50. Reseda, F.U.B. Landsat 8. Available online: https://blogs.fu-berlin.de/reseda/landsat-8/ (accessed on 11 December 2023).
51. de Responsabilidad Fiscal, A.I. ESTUDIO INFRAESTRUCTURAS DE TRANSPORTE. ANEXO 1, La inversión y el stock de infraestructuras de transporte en España. Jul. 2020. Available online: https://www.airef.es/wp-content/uploads/2020/07/INFRAESTRUCTURAS/Anexo-1_La-inversion-y-el-stock-de-infraestructuras-de-transporte-en-Espa%C3%B1a.pdf (accessed on 18 June 2024).
52. Demuzere, M.; Bechtel, B.; Middel, A.; Mills, G. Mapping Europe into local climate zones. *PLoS ONE* **2019**, *14*, e0214474. [CrossRef] [PubMed]
53. Soriano, P. Spanish Inspire Catastral Downloader—QGIS Python Plugins Repository. Available online: https://plugins.qgis.org/plugins/Spanish_Inspire_Catastral_Downloader/ (accessed on 25 April 2023).
54. Demuzere, M.B.B.; Hankey, S.; Mills, G.; Zhang, W.; Lu, T. LCZ resources–World Urban Database. Available online: https://www.wudapt.org/lcz-resources/ (accessed on 18 May 2023).
55. Barane, G.S.D.P. NITK_RS-GIS_17/LST_Calculation.pdf at master · PrathamGitHub/NITK_RS-GIS_17 · GitHub. Available online: https://github.com/PrathamGitHub/NITK_RS-GIS_17/blob/master/LST_Calculation.pdf (accessed on 19 May 2023).
56. Ferretti, A.; Prati, C.; Rocca, F. Nonlinear subsidence rate estimation using permanent scatterers in differential SAR interferometry. *IEEE Trans. Geosci. Remote Sens.* **2000**, *38*, 2202–2212. [CrossRef]

57. USGS. InSAR—Satellite-Based Technique Captures Overall Deformation 'Picture' | U.S. Geological Survey. Available online: https://www.usgs.gov/programs/VHP/insar-satellite-based-technique-captures-overall-deformation-picture (accessed on 19 May 2023).
58. Shaked, M.; Joe, H. Multivariate Models and Dependence Concepts. *J. Am. Stat. Assoc.* **1998**, *93*, 1237. [CrossRef]
59. Morales-Nápoles, O.; Delgado-Hernández, D.J.; De-León-Escobedo, D.; Arteaga-Arcos, J.C. A continuous Bayesian network for earth dams' risk assessment: Methodology and quantification. *Struct. Infrastruct. Eng.* **2014**, *10*, 589–603. [CrossRef]
60. Schober, P.; Schwarte, L.A. Correlation coefficients: Appropriate use and interpretation. *Anesth. Analg.* **2018**, *126*, 1763–1768. [CrossRef] [PubMed]
61. Headrick, T.C. A Note on the Relationship between the Pearson Product-Moment and the Spearman Rank-Based Coefficients of Correlation. *Open J. Stat.* **2016**, *06*, 1025–1027. [CrossRef]
62. Mendoza-Lugo, M.A.; Morales-Nápoles, O.; Delgado-Hernández, D.J. A Non-parametric Bayesian Network for multivariate probabilistic modelling of Weigh-in-Motion System Data. *Transp. Res. Interdiscip. Perspect.* **2022**, *13*, 100552. [CrossRef]
63. Hanea, A.; Napoles, O.M.; Ababei, D. Non-parametric Bayesian networks: Improving theory and reviewing applications. *Reliab. Eng. Syst. Saf.* **2015**, *144*, 265–284. [CrossRef]
64. Paprotny, D.; Morales-Nápoles, O.; Worm, D.T.H.; Ragno, E. BANSHEE–A MATLAB toolbox for Non-Parametric Bayesian Networks. *SoftwareX* **2020**, *12*, 100588. [CrossRef]
65. Koot, P.; Mendoza-Lugo, M.A.; Paprotny, D.; Morales-Nápoles, O.; Ragno, E.; Worm, D.T.H. PyBanshee version (1.0): A Python implementation of the MATLAB toolbox BANSHEE for Non-Parametric Bayesian Networks with updated features. *SoftwareX* **2023**, *21*, 101279. [CrossRef]
66. Hu, L.; Brunsell, N.A. The impact of temporal aggregation of land surface temperature data for surface urban heat island (SUHI) monitoring. *Remote Sens. Environ.* **2013**, *134*, 162–174. [CrossRef]
67. Sharifi, A.; Yamagata, Y. Resilient Urban Planning: Major Principles and Criteria. *Energy Procedia* **2014**, *61*, 1491–1495. [CrossRef]